Sakarya Üniversitesi Fen Bilimleri Dergisi
Sakarya University Journal of Science

e-ISSN : 2147-835X
Publisher : Sakarya University

Vol. 29, No. 4, 363-382, 2025
DOI: https://doi.org/10.16984/saufenbilder.1681034

Research Article

Crystallization of Biogenic Hydroxyapatite: Phase Purity and Morphological Control via Successive Annealing and Grinding

H. Esma Okur

Bursa Technical University, Faculty of Engineering and Natural Sciences, Department of Chemistry, Bursa, Türkiye, esma.okur@btu.edu.tr, ror.org/03rdpn141

ARTICLE INFO

Keywords:
Biogenic hydroxyapatite
Solid-state crystallization
Successive annealing
Thermal optimization
Rietveld refinement

ABSTRACT

Hydroxyapatite (HAp) derived from biogenic sources offers a sustainable and cost-effective alternative to synthetic materials, yet controlling its crystal structure and morphology remains a key challenge. In this study, polycrystalline HAp is extracted from alkali-treated fish scales and subjected to a carefully designed solid-state crystallization protocol involving successive annealing at 320 °C, 500 °C, 600 °C, 700 °C, and 800 °C, with intermediate manual grinding steps. This multi-step thermal approach addresses the limitations of conventional one-step calcination and enables controlled structural evolution. X-ray powder diffraction analyzed via Rietveld refinement reveals a progressive enhancement in crystallinity and phase purity with increasing temperature, with no detectable secondary phases. Well-defined hexagonal facets emerge at 800 °C, indicating advanced structural ordering. Scanning electron microscopy shows a transition from loosely aggregated, irregular clusters to uniform, faceted grains. Fourier-transform infrared spectroscopy confirms the presence of phosphate, hydroxyl, and trace carbonate groups, with carbonate bands decreasing at higher temperatures. Semi-quantitative energy-dispersive X-ray spectroscopy supports carbonate incorporation and suggests trace localized magnesium, without clear evidence of significant elemental substitution. Compared to direct calcination, successive annealing improves thermal regulation, minimizes agglomeration, and preserves nanostructural integrity—features essential for biomedical and catalytic applications. The combined use of alkali pre-treatment, stepwise annealing, and intermediate grinding results in a tunable, solid-state route for tailoring the crystal structure and morphology of biogenic HAp. This optimized method enables the synthesis of phase-pure HAp at moderate temperatures and presents a scalable pathway for advanced applications in bioceramics, environmental remediation, and sustainable materials engineering.

Article History:
Received: 21.04.2025
Revised: 25.06.2025
Accepted: 21.07.2025
Online Available: 11.08.2025

1. Introduction

The increasing global focus on sustainable technologies has drawn attention to the conversion of biogenic waste into value-added materials. Among these, fish scales—an abundant by-product of the fishing and seafood processing industries—are frequently discarded, contributing to environmental waste streams [1, 2]. Yet, they are a rich natural source of functional compounds with potential applications across diverse fields, including the extraction of collagen, hydroxyapatite (HAp), guanine, and their use in fertilizers, cosmetics, biomedical materials, and adsorbents [3]. Among calcium phosphate minerals, hydroxyapatite ($Ca_{10}(PO_4)_6(OH)_2$, HAp) has gained particular attention as a bioceramic of considerable importance due to its close structural similarity to the mineral phase of human bone and teeth. Calcium phosphate (CaP) compounds are composed of calcium cations (Ca^{2+}) and phosphate-based anions such as PO_4^{3-}, PO_3^{-}, or $P_2O_7^{4-}$, often incorporating hydroxyl (OH^{-}) or hydrogen (H^{+}) ions. Naturally abundant in phosphate rock deposits, CaP minerals play an essential role in biological systems as the primary inorganic constituents of skeletal tissues and

Cite as: H. E. Okur, “Crystallization of biogenic hydroxyapatite: Phase purity and morphological control via successive annealing and grinding,” Sakarya University Journal of Science, vol. 29, no. 4, pp. 363-382, 2025. https://doi.org/10.16984/saufenbilder.1681034

pathological calcifications. Since its early identification in 1769, hydroxyapatite has remained a subject of intensive research, particularly in materials science and biomedical engineering, due to its chemical compatibility with hard tissues [4–6].

In biological tissues, HAp constitutes approximately 60% of the inorganic matrix of bone and nearly 90% of tooth enamel [7]. Its remarkable biocompatibility, bioactivity, and osteoconductivity have established HAp as one of the most widely used bioceramics in biomedical applications, including bone grafts, dental implants, and drug delivery systems [8–14]. Beyond its biomedical role, HAp has also been employed in environmental and industrial fields due to its high adsorption capacity, chemical stability, and ion-exchange properties—making it effective in water purification, catalysis, and heavy metal removal [15–17].

Despite its broad applicability, extracting high-purity hydroxyapatite from natural sources poses several challenges, particularly with respect to achieving structural stability and phase purity. The physicochemical characteristics of biogenic HAp are highly sensitive to factors such as synthesis parameters, thermal treatment protocols, and the composition of the raw material. These complexities highlight the need for carefully optimized processing strategies to obtain structurally stable, phase-pure HAp suitable for advanced biomedical and environmental applications.

HAp exists in two crystallographic forms: a hexagonal system (space group $P6_3/m$) with lattice parameters $a = b = 9.432$ Å, $c = 6.881$ Å [18] and a monoclinic system (space group $P2_1/b$) featuring $a = 9.4214(8)$ Å, $b = 2a$, $c = 6.8814(7)$ Å, and $\gamma = 120°$ [19]. Although both forms share a stoichiometric Ca/P ratio of 1.67, achieving this ideal composition can be challenging—particularly for biogenic HAp—due to variations in source materials and processing conditions. In the commonly encountered hexagonal HAp lattice ($P6_3/m$), two distinct types of calcium ions, Ca(I) and Ca(II), occupy separate structural channels and coordination sites [17]. Ca(I) resides in so-called B-type channels, forming a tricapped trigonal prismatic arrangement with nine coordinating oxygen atoms, whereas Ca(II) is located in A-type channels with seven oxygen neighbors in a distorted pentagonal bipyramidal geometry. The structural backbone consists of phosphate groups (PO_4^{3-}), with each phosphorus atom tetrahedrally coordinated to four oxygen atoms, and hydroxyl ions (OH^-) aligned along the channel centers, stabilizing the lattice along the *c*-axis. Because Ca(I) and Ca(II) sites along the *a*-axis are relatively flexible, moderate thermal expansion is accommodated in that direction, whereas the more rigid, Ca(II)-dominated channels along the *c*-axis limit expansion at elevated temperatures.

Additionally, HAp can transition from its ideal formula, $Ca_{10}(PO_4)_6(OH)_2$, to calcium-deficient variants, $Ca_{10-x}(HPO_4)_x(PO_4)_{6-x}(OH)_{2-x}$, by adjusting the Ca/P ratio—yet still retain its overarching hexagonal framework [20–23]. Such nonstoichiometry, prevalent in natural apatites like those in bone and teeth [21], introduces vacant Ca^{2+} sites that markedly affect properties such as ion exchange and sorption, underscoring the importance of Ca/P control in tailoring HAp for biomedical and environmental applications.

Conventional synthesis of HAp often relies on chemical methods such as wet chemical precipitation, sol-gel processes, and hydrothermal techniques [24]. Although effective, these approaches can be costly, energy-intensive, and environmentally taxing, partly because they require chemically pure starting materials and involve multiple complex processing steps. In response, natural, renewable sources like fish scales, eggshells, and animal bones have emerged as sustainable alternatives. Fish scales, in particular, represent an abundant and low-cost by-product of the seafood industry [3, 25]. With proper extraction methods, they can be transformed into high-purity HAp, addressing both environmental sustainability and the growing demand for high-performance biomaterials.

Various experimental approaches have been developed to extract biogenic HAp, with outcomes largely shaped by both the origin of the natural precursor and the thermal processing conditions applied. These variables have a direct influence on key material characteristics, including elemental composition (e.g., Ca/P ratio), degree of crystallinity, phase assemblage, particle morphology, and thermal stability [26–32]. For instance, a recent study [33] showed that variations in air exposure during calcination affect the color and optical properties of HAp derived from fish scales, without modifying its underlying crystal structure—underscoring the critical role of thermal environment in tuning surface features.

For fish scale-derived HAp, organic removal is particularly crucial, and specialized methods—including enzymatic, acidic, alkaline, or thermal treatments—are typically required [34–37]. While some of these techniques can be time-consuming and resource-intensive [3], recent advancements underscore the effectiveness of alkali heat treatment, which combines alkaline hydrolysis with controlled heating [38–40]. This method has been shown to enhance crystallization while minimizing secondary phase formation, such as tricalcium phosphate (TCP) or β-TCP, which frequently appear in direct calcination methods [41–45].

Indeed, direct calcination is a widely used method for transforming fish scales into crystalline HAp. However, previous studies [17] and [33] demonstrated that while this approach effectively converts the biogenic precursor into HAp, it often results in significant particle aggregation, irregular morphology, and the formation of magnesium whitlockite as a secondary phase. These observations highlight the need for a more controlled thermal strategy to enhance crystallinity, particle uniformity, and phase purity. To address these challenges, the present study applies a successive annealing approach with intermittent grinding, a methodology successfully implemented in the synthesis of A_3C_{60} ternary superconducting fullerides [46] for optimizing structural and electronic properties. Here, this strategy is adapted for biogenic HAp—a protocol not previously applied to HAp derived from fish scales. By integrating alkali pre-treatment with stepwise thermal annealing and periodic grinding, this work seeks to overcome the limitations of direct calcination. Notably, both [17] and [33] used fish scales sourced from the same supplier, ensuring that the improvements observed in this study result from modified processing conditions rather than variations in raw material composition.

The primary objective of this study is to establish a scalable and sustainable protocol for producing high-purity, single-phase hydroxyapatite from fish scales at moderate temperatures, while simultaneously exploring the role of particle coalescence in enhancing crystallinity and structural organization. In contrast to the direct calcination approach used in previous work [17], the current work applies successive annealing combined with intermediate grinding, enabling a stepwise and controlled thermal treatment that promotes gradual particle growth, improved ordering, and reduced phase impurities. The successful formation of hexagonal faceted crystals at 800 °C—significantly lower than the typical calcination temperatures reported for biogenic HAp (e.g., 1000 °C) [47], demonstrates the effectiveness of this thermally optimized, solid-state strategy.

By employing Rietveld refinement, this study offers quantitative and reliable crystallographic insights into the structural evolution of HAp during successive annealing, enabling precise tracking of key parameters such as the Ca/P ratio, lattice constants, atomic positions, and phase composition. Complementary scanning electron microscopy provides a comprehensive assessment of morphological changes, particularly the progression of particle coalescence and faceting with increasing annealing temperature. Together, these techniques support the optimization of fish scale-derived HAp while showcasing a sustainable strategy for transforming biogenic waste into high-performance biomaterials for biomedical and environmental applications. Comparisons with direct calcination further underscore the advantages of the successive annealing method in achieving enhanced crystallinity and controlled particle morphology.

2. Materials and Methods

2.1. Extraction of hydroxyapatite powder from European seabass scales

Hydroxyapatite (HAp) was extracted from European seabass (*Dicentrarchus labrax*) scales, obtained as a by-product from Bursa Kocamanlar Seafood. The scales were thoroughly washed with water, dried in shadow, and subjected to a sequential chemical treatment to remove organic components. 60 g of fish scales were soaked in 80 mL of 0.1 M hydrochloric acid (HCl) for 30 minutes under intermittent stirring. The treated scales were then filtered and washed with deionized water.

The deproteinized scales were immersed in 5% (w/v) sodium hydroxide (NaOH) and refluxed at 70°C with continuous stirring (250 rpm for 2 hours, followed by 450 rpm for another 2 hours). After filtration and washing, the scales were subjected to a second NaOH treatment (50% w/v) at 100°C for 30 minutes at 250 rpm. The neutralized material was dried at 60°C, scraped, and collected. The dried powder sieved through a 150 µm mesh to ensure uniform particle size. The sieved HAp powder was divided into two portions: one was analyzed without thermal treatment and labeled as ‘Alkali,’ while the other underwent successive thermal treatments to optimize crystallization.

The same batch of fish scales used in [17] was employed here, where comprehensive analyses of the raw scales—including thermogravimetric assessment—are detailed in the Electronic Supplementary Information (ESI) of [17]. Those findings confirmed 800 °C as an optimal processing temperature to ensure effective removal of organic residues. Building on this initial characterization, the present work integrates alkali pre-treatment followed by stepwise thermal optimization up to 800 °C, further refining and validating the transformation of the raw scales into high-purity HAp.

2.2. Thermal optimization

The white powder obtained after alkali treatment was subjected to two thermal protocols: successive annealing and direct annealing. For successive annealing, the sample was first heated to 320 °C (A-320) to assess crystallinity by X-ray powder diffraction (XRPD). As further heating was required for HAp phase formation, the same sample underwent additional stepwise annealing at 500, 600, 700, and 800 °C for 2 hours each, at a ramp rate of 10 °C/min. These samples were labeled A-500, A-600, A-700, and A-800, respectively. After each step, the powder was manually ground before XRPD analysis to monitor structural evolution.

In the direct annealing protocol, separate portions of alkali-treated powder were heated directly to 700 °C and 800 °C without intermediate steps or grinding. These were labeled AD-700 and AD-800, where ‘AD’ denotes alkali-treated powder subjected to direct annealing. The key distinction between these protocols lies in the thermal trajectory: successive annealing allows gradual atomic reorganization, enhancing crystallinity, while direct annealing serves as a reference for rapid, one-step heat treatment.

Although the terms calcination, sintering, and annealing are often used interchangeably, ‘annealing’ is most appropriate here. Unlike calcination, which typically burns off organics at high temperatures, or sintering, which promotes densification, the stepwise heating used here (320–800 °C) was designed to enhance crystallinity, minimize defects, and promote lattice organization without decomposition. The alkali pre-treatment ensured organics were removed prior to heating, further distinguishing this method from conventional calcination.

2.3. Structural characterizations

2.3.1. X-ray powder diffraction (XRPD)

XRPD patterns were collected at room temperature using a Bruker D8 Advance diffractometer in Bragg–Brentano geometry, employing Cu Kα radiation (λ = 1.54056 Å). Data were recorded over a 2θ range of 5–60° with a step size of 0.02°. Structural analysis was performed on the 10–60° range using Rietveld refinement with the GSAS software suite [48]. Peak profiles were modeled using a pseudo-Voigt function [49], which combines Gaussian and Lorentzian components, while peak integration was carried out via multi-term

Simpson's rule [50]. Background intensities were fitted with a Chebyshev polynomial due to its minimax property, which balances oscillation control and fitting accuracy—especially effective for fine-grained powders.

Rietveld refinement enabled the extraction of lattice constants, atomic positions, unit cell volumes, and phase fractions. Unlike traditional peak-fitting methods, this whole-pattern approach allows for precise modeling of lattice distortions and secondary phase quantification. Anomalous scattering factors (f' and f'') were computed using DISPANO [51] and applied to improve occupancy refinement.

Refinement proceeded iteratively, optimizing zero-point errors, background, peak broadening, unit cell dimensions, and atomic displacement factors. Atomic positions were refined when necessary, with constraints applied to maintain physical consistency. The quality of the refinement was evaluated using the weighted profile R-factor (R_{wp}) and the expected R-factor (R_{exp}), and goodness-of-fit (χ^2) parameter serving as a key indicator of refinement accuracy. While a χ^2 value close to 1 generally suggests a well-fitted structural model, some deviations may arise due to sample-dependent effects such as preferred orientation, residual strain, or instrumental broadening.

2.3.2. Fourier transform infrared spectroscopy (FTIR)

Fourier transform infrared (FTIR) spectroscopy was conducted using a Thermo Nicolet iS50 spectrometer equipped with a diamond Attenuated Total Reflectance (ATR) accessory. Spectra were collected over the 4000–400 cm^{-1} range to monitor the evolution of functional groups in HAp powders at various stages of the successive annealing and grinding process.

2.3.3. Scanning electron microscopy (SEM)/energy dispersive X-ray spectroscopy (EDS)

The morphology of the powders was evaluated using SEM on a Zeiss Gemini 300 microscope, equipped with a Bruker XFlash 6I100 EDS detector (operating in In-Lens mode). Prior to imaging, samples were coated with a 15 nm Au–Pd (60:40) alloy using a Leica EM ACE600 high-vacuum coater. EDS spot analyses and elemental mapping were performed primarily to confirm the presence and distribution of key elements (e.g., Ca, P, O) and possible dopants (C, Na, Mg). Because EDS is semi-quantitative, these measurements served mainly to verify elemental content rather than to establish precise stoichiometric ratios or quantify trace substitutions.

2.3.4. Brunauer–Emmett–Teller (BET) surface area analysis

Specific surface area measurements were performed using nitrogen adsorption–desorption isotherms on a Micromeritics TriStar II 3020 analyzer. All samples were degassed under vacuum prior to analysis to eliminate adsorbed contaminants. Measurements were conducted at 77.35 K using nitrogen (N_2) as the adsorptive gas, and the BET surface area was calculated using the multi-point method in the relative pressure (p/p^0) range of 0.05–0.30.

BET analysis was carried out on four representative samples: the alkali-treated powder (Alkali, unannealed), successively annealed powders at 600 °C (A-600) and 800 °C (A-800), and the directly annealed powder at 800 °C (AD-800). This selection was chosen to evaluate the evolution of surface area in relation to thermal treatment and annealing protocol.

3. Results

3.1. Qualitative analysis of the XRPD data

XRPD patterns of alkali-treated HAp powders annealed at 320–800 °C are shown in Figure 1. The untreated 'Alkali' sample exhibits broad, low-intensity peaks, consistent with low crystallinity and small grain size. With increasing annealing temperature, the Bragg peaks sharpen and intensify, reflecting improved crystallinity and progressive grain growth.

Key reflections between $2\theta = 31.7°$ and $34.1°$, corresponding to (121), (211), (112), (030), and (022) planes of hexagonal HAp ($P6_3/m$), become well-defined at ≥ 600 °C.

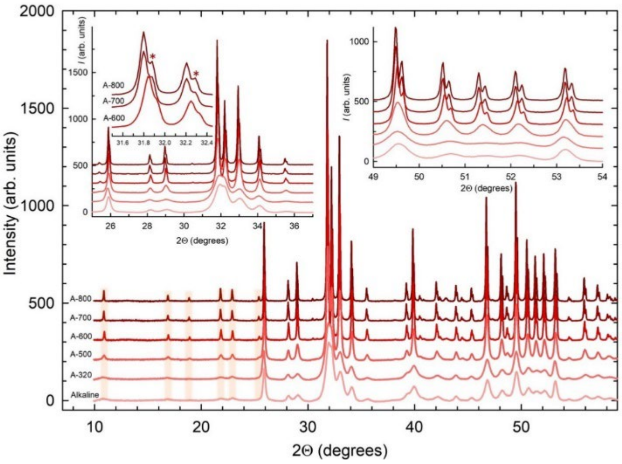

Figure 1. XRPD patterns of the powders obtained after alkali pre-treatment followed by successive annealing at various temperatures. The 'A' label represents the powder after alkali pre-treatment without heat treatment. The labels A-320, A-500, A-600, A-700, and A-800 correspond to powders annealed at 320°C, 500°C, 600°C, 700°C, and 800°C, respectively, for 2 hours. The insets highlight the evolution of the most prominent HAp peaks, with increased sharpness and crystallinity as annealing temperature rises. Asterisks (*) mark discernible shoulders at 700°C and 800°C. Colored rows focus attention on low-angle peaks that emerge with increasing temperature, reflecting enhanced crystallization

The insets in Figure 1 highlight both increased peak intensity and a subtle shift of major peaks to lower angles between 600 and 800 °C, suggesting unit cell expansion linked to enhanced atomic ordering. This trend, together with earlier thermal analyses in [17], supports the identification of 800 °C as the optimal annealing temperature for this specific material.

Figure 2 compares powders annealed at 700 and 800 °C using both successive and direct protocols. At 700 °C, the (211) peak is more defined in A-700, appearing as a clear shoulder, while it remains less resolved in AD-700—indicating superior crystallization via successive annealing. At 800 °C, both A-800 and AD-800 show comparable peak intensity and shape, though a minor shift to lower 2θ in A-800 suggests slightly greater lattice expansion. These results indicate that gradual thermal treatment fosters more uniform crystal growth and long-range order. Rietveld refinement will follow to confirm these structural trends quantitatively.

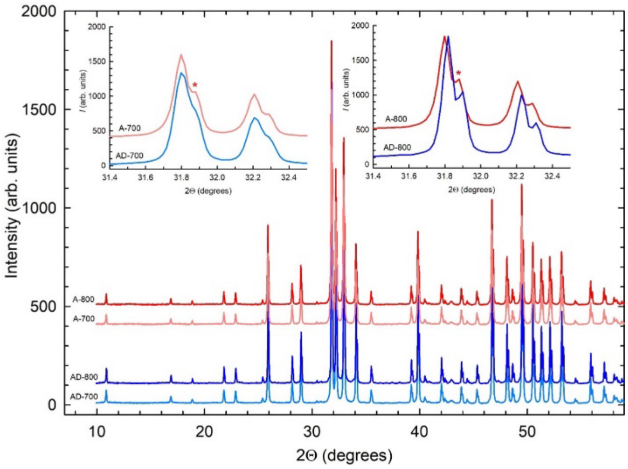

Figure 2. XRPD patterns comparing powders after successive (A-700, A-800; represented by red lines) and direct annealing (AD-700, AD-800; represented by blue lines) at 700°C and 800°C. The insets provide a closer view of the (211) peak for each sample, with asterisks (*) marking discernible shoulders

3.2. Rietveld analysis of the XRPD data

Figure 3 shows the Rietveld fits to the XRPD patterns of HAp powders subjected to successive annealing after alkali pre-treatment. The results confirm the successful formation of single-phase, well-crystallized biogenic HAp with no detectable secondary phases. Samples annealed at 500°C, 600°C, 700°C, and 800°C were refined using the hexagonal $P6_3/m$ (no. 176) [52] which accounted for all observed reflections. The absence of 00*l* (*l* odd) reflections further supports the assignment to this symmetry. Scattering factor corrections for anomalous dispersion (f' and f'') were applied in GSAS using the following values: Ca $f' = 0.340$, $f'' = 1.235$; P $f' = 0.283$, $f'' = 0.433$, and O $f' = 0.046$, $f'' = 0.032$.

The extraction of single-phase, well-crystalline biogenic HAp from alkali-treated fish scales followed by annealing highlights the importance of chemical treatment over direct calcination, which often leads to the formation of secondary phases such as β-tricalcium phosphate (β-TCP, $Ca_3(PO_4)_2$) or magnesium whitlockite ($Ca_{18}Mg_2H_2(PO_4)_{14}$) [17], [33], [44], [53–55].

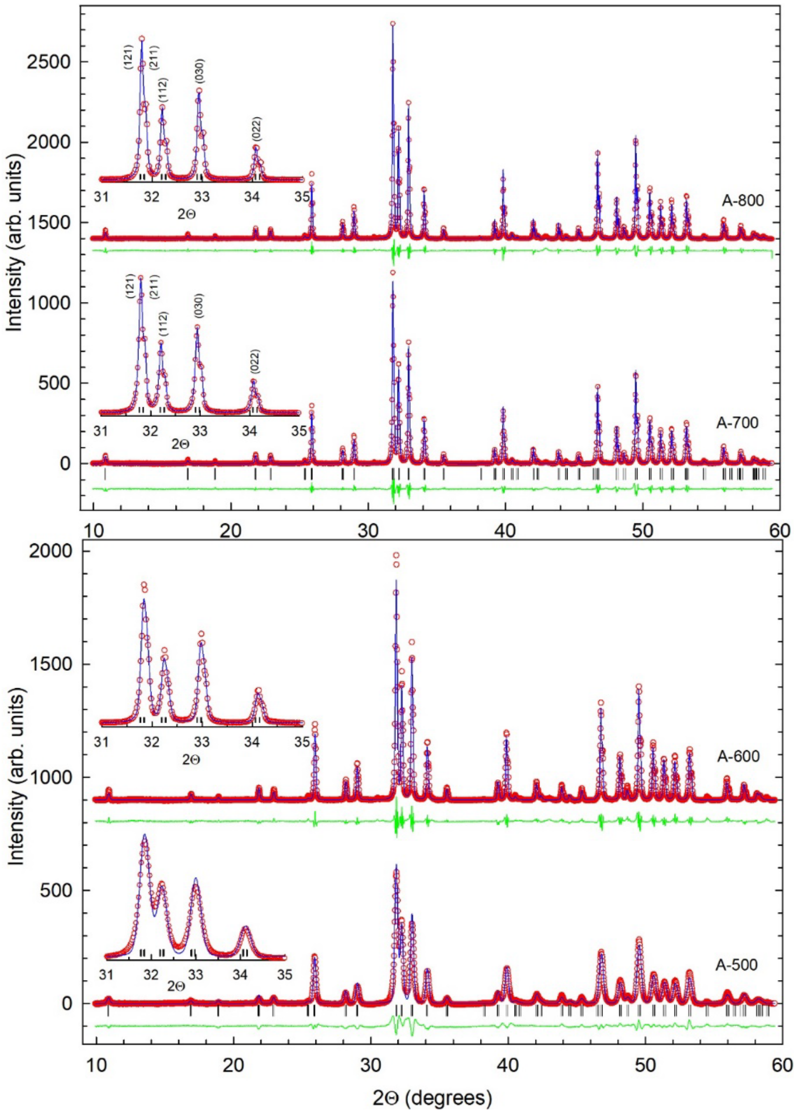

Figure 3. Rietveld fits to XRPD data for the powders obtained after alkali pre-treatment followed by successive annealing from bottom to up at 500°C, 600°C, 700°C, and 800°C, collected at ambient temperature with $\lambda = 1.5406$ Å. The red circles, blue lines and green lines represent the observed data, the calculated profile, and the difference between observed and calculated profiles, respectively. Black ticks mark the reflection positions of hexagonal hydroxyapatite $Ca_{10}(PO_4)_6(OH)_2$ (space group $P6_3/m$). The insets highlight the most prominent reflections for $2\theta = 31°\text{-}35°$, illustrating enhanced peak sharpness and crystallinity as the annealing temperature increases

Because biogenic HAp often deviates from the ideal Ca/P ratio, partial substitutions at the Ca sites (A- and B-type) by Na^+ and Mg^{2+} (to simulate Ca deficiency), as well as the incorporation of CO_3^{2-} at phosphate sites, were tested in the refinement model. However, no noticeable improvement in the *R*-factors or overall refinement quality resulted from these modifications. EDS measurements conducted in this study confirmed the presence of C, aligning with FTIR evidence of CO_3^{2-} substitution. Although Na and Mg were not detected in the EDS spectra, EDS mapping revealed localized Mg-rich regions, suggesting that Mg is present at low concentrations but heterogeneously distributed rather than uniformly substituting into the HAp lattice. The lack of Na and weak Mg signal in the EDS spectra does not necessarily indicate their absence but rather their low detectability due to the detection limits of EDS, particularly for lighter elements in a Ca/P-dominant matrix.

A comparison with previous findings further supports these observations. In [17], where direct calcination was applied at 800°C without any pre-treatment (i.e., no alkali pre-treatment or boiling step), no CO_3^{2-} bands were observed in the FTIR spectra. However, EDS still detected carbon at 3.81(±2.99)%, suggesting that C may have been present in a non-structural form (e.g., adsorbed species or residual carbon from incomplete organic decomposition) rather than incorporated into the HAp lattice. In contrast, in the present study, where an alkali pre-treatment was introduced before annealing, both EDS and FTIR consistently indicate carbonate incorporation, suggesting that the processing route influences whether carbon remains as an external contaminant or integrates into the HAp structure as CO_3^{2-}.

Despite these findings, introducing these dopants into the Rietveld model did not significantly alter the refined structural parameters. This is likely due to their low concentrations and the inherent limitations of lab-based XRPD, which struggles to resolve light elements (especially C) and minor substitutions with similar atomic scattering factors. Neutron diffraction, which interacts with atomic nuclei rather than electron clouds, is a more suitable technique for detecting light elements such as O, C, and H. Additionally, complementary spectroscopic methods, such as Raman spectroscopy or solid-state NMR, could provide further confirmation of CO_3^{2-} incorporation and potential Mg substitution in the HAp lattice.

Refinement of the hexagonal HAp unit cell parameters at 500 °C yielded $a = b = 9.4124(2)$ Å, $c = 6.8878(2)$ Å, and $V = 528.45(2)$ Å^3. At 800 °C, the values shifted to $a = b = 9.42086(6)$ Å, $c = 6.88613(7)$ Å, and $V = 529.282(6)$ Å^3, indicating a minor elongation along the a-axis and a subtle contraction along c. This corresponds to an overall volume expansion of approximately 0.16%, reflecting enhanced atomic ordering and the relaxation of structural vacancies or local distortions with increasing temperature.

These findings are in close agreement with previous studies [17, 33], though the slight differences observed here likely arise from the alkali pre-treatment and stepwise annealing, which promote more controlled crystal growth and lattice relaxation. The anisotropic behavior observed in the unit cell can be attributed to the structural arrangement of the HAp lattice. The a-axis is populated by Ca(I) and Ca(II) ions coordinated to PO_4^{3-} groups, affording some flexibility for thermal expansion.

In contrast, the c-axis features more rigid A-type channels, where Ca(II) ions form pentagonal bipyramidal coordination around OH^- groups, limiting thermal expansion in that direction.
To ensure chemically reasonable values for light atoms like O, P–O bond lengths were restrained to 1.55 ± 0.05 Å with high weighting. Following this, the site multiplicities of Ca(1) and Ca(2) were freely refined, while the positions of O(4) and H (within hydroxyl groups) were fixed to literature-reported values [52].

Table 1 shows how P–O distances evolve with temperature: for example, P–O1 expands from 1.530(6) Å at 500 °C to 1.578(6) Å at 600 °C, then contracts to 1.535(18) Å at 800 °C. P–O2 decreases steadily from 1.693(4) Å at 500 °C to 1.619(6) Å at 700 °C, followed by a slight increase to 1.623(6) Å at 800 °C. Similarly, P–O3 contracts from 1.722(3) Å at 500 °C to 1.694(2) Å at 600 °C, before showing a modest expansion at higher temperature. These non-monotonic shifts likely reflect dynamic reorganization of the phosphate groups, with thermally driven relaxation and local ordering processes balancing each other. Although typical P–O distances in synthetic HAp fall between 1.529 and 1.545 Å [52], the slightly elongated values observed here—even under restraint—suggest mild structural distortions, potentially due to ionic substitutions, lattice defects, or microstructural changes induced by the applied thermal and mechanical treatments.

To gain insight into atomic vibrations, atomic displacement parameters were refined. Both isotropic and anisotropic models were tested; however, neither yielded fully reliable results, likely due to limitations of laboratory-based X-ray diffraction in resolving light atoms such as oxygen and hydrogen. These issues are consistent with prior studies, where X-ray-derived thermal parameters for phosphate-bound oxygen atoms were often overestimated compared to neutron data [52]. To address this, thermal parameters from neutron diffraction studies were used as references, and only site occupancies were refined to capture the chemical behavior of light elements in biogenic HAp. The presence of minor dopants such as CO_3^{2-}, Mg^{2+}, and Na^{+} can distort occupancies and local vibrations, further complicating refinement [56].

Table 1. Refined structural parameters for hexagonal hydroxyapatite (space group $P6_3/m$) from Rietveld analysis of XRPD data collected at ambient temperature from the successively annealed powders with $\lambda = 1.5406$ Å

Structural parameters	500°C	600°C	700°C	800°C
$a = b$ (Å)	9.4124(2)	9.42113(8)	9.41996(7)	9.42086(6)
c (Å)	6.8875(2)	6.88762(9)	6.88578(9)	6.88613(7)
V (Å^3)	528.44(2)	529.43(1)	529.15(1)	529.282(6)
P−O1 (Å)	1.530(6)	1.578(6)	1.56(15)	1.535(18)
P−O2 (Å)	1.693(4)	1.621(4)	1.619(6)	1.623(6)
P−O3 (Å)	1.722(3)	1.694(2)	1.700(5)	1.695(4)

Table 2 lists the refined crystallographic parameters obtained through Rietveld analysis of the successively annealed samples, including site multiplicities, occupancies, and overall stoichiometry. These results support the preservation of the hexagonal structure and confirm consistent compositional refinement with increasing annealing temperature. Overall, this Rietveld analysis confirms that optimized annealing protocols and chemical pre-treatment enhance phase purity, crystallinity, and stoichiometric balance in biogenic HAp. While lab-based XRPD provides valuable structural information, complementary techniques like neutron diffraction or solid-state spectroscopy are needed to resolve light-element sites and subtle substitutions more reliably.

3.3. FTIR

Figure 4 presents the FTIR spectra of the HAp samples over the 400–4000 cm^{-1} range, highlighting the vibrational modes of PO_4^{3-}, OH^-, and CO_3^{2-} groups. The PO_4^{3-} ion displays four main IR-active modes: symmetric stretching (ν_1) at ~960 cm^{-1}, symmetric bending (ν_2) at ~472 cm^{-1}, antisymmetric stretching (ν_3) at ~1027 and 1086 cm^{-1}, and antisymmetric bending (ν_4) at ~564 and 605 cm^{-1} [57]. The OH^- stretching vibration appears at ~3600 cm^{-1}, while its librational mode is observed near 630 cm^{-1}, confirming that OH^- is structurally incorporated into the HAp lattice rather than merely adsorbed on the surface [57].

Trace amounts of CO_3^{2-} are evidenced by bands at ~1450 and 1415 cm^{-1} (ν_3) and 875 cm^{-1} (ν_2 out-of-plane bending), indicating B-type substitution where CO_3^{2-} replaces PO_4^{3-} in the lattice [58- 59]. The absence of bands around 1455 and ~1540 cm^{-1} suggests that A-type substitution (CO_3^{2-} replacing OH^-) is minimal [60].

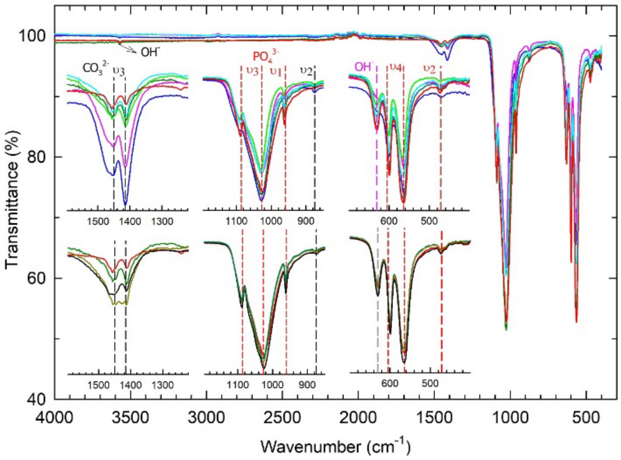

Figure 4. FTIR spectra of HAp powders prepared by successive annealing (A series) and direct annealing (AD series). Labeled characteristic bands include PO_4^{3-} (red dashed), CO_3^{2-} (black dashed), and OH^- librational mode (pink dashed). The upper inset shows successive samples from 320°C to 800°C (Alkali: blue, A-320: pink, A-500: green, A-600: cyan, A-700: dark green, A-800: red). The lower inset compares A-700/A-800 (dark green/red) with AD-700/AD-800 (dark yellow/black), illustrating carbonate band variations

Although EDS supports the presence of carbon, precise localization of CO_3^{2-} substitution (A-, B-, or AB-type) would require advanced techniques such as ^{13}C NMR or neutron diffraction. As annealing temperature increases, the carbonate bands progressively diminish, reflecting thermal decomposition and gradual CO_2 release. In the successively annealed (A-series) samples, intermediate grinding enhances this process by exposing fresh surfaces and promoting carbonate elimination. This is particularly evident when comparing A-700 and A-800 with their direct annealing counterparts (AD-700, AD-800), where CO_3^{2-} bands remain more intense.

Table 2. Refined stoichiometry, site multiplicities (column *M*) and occupancies (column *N*) for hexagonal hydroxyapatite (space group $P6_3/m$), obtained from Rietveld refinement of XRPD data collected at ambient temperature using Cu Kα radiation (λ = 1.5406 Å) from successively annealed powders. Values in parentheses represent estimated standard deviations from the least-squares fitting. The weighted profile and expected R-factors are also listed as R_{wp} and R_{exp} respectively.

800°C Refined stoichiometry: $Ca_{9.56(3)}P_{6.00(4)}O_{25.5(1)}(OH)_{2.58(3)}$; Ca/P: 1.59(1); R_{wp} = 3.70%, R_{exp} = 1.56%

Atoms	*x/a*	*y/b*	*z/c*	*M*	*N*
Ca(1)	0.3333	0.6667	0.0096(8)	4	0.906(5)
Ca(2)	0.2460(3)	0.9877(4)	0.25	6	0.989(4)
P	0.4013(8)	0.3665(6)	0.25	6	1.000(6)
O(1)	0.303(1)	0.457(1)	0.25	6	1.00(1)
O(2)	0.6010(8)	0.482(2)	0.25	6	1.33(1)
O(3)	0.3345(6)	0.5030(4)	0.0505(5)	12	0.959(5)
O-h	0	0	0.201886	4	0.644(7)
H	0	0	0.057462	4	0.644(7)

700°C Refined stoichiometry: $Ca_{9.56(3)}P_{6.07(3)}O_{25.9(2)}(OH)_{2.58(3)}$; Ca/P: 1.58(1); R_{wp} = 3.75%, R_{exp} = 1.55%

Atoms	*x/a*	*y/b*	*z/c*	*M*	*N*
Ca(1)	0.3333	0.6667	0.0095(7)	4	0.999(3)
Ca(2)	0.24595(28)	0.98734(32)	0.25	6	0.963(3)
P	0.4013(7)	0.3668(6)	0.25	6	1.011(5)
O(1)	0.3010(13)	0.4572(9)	0.25	6	1.01(1)
O(2)	0.5993(8)	0.478(2)	0.25	6	1.34(2)
O(3)	0.3342(6)	0.2454(4)	0.0496(5)	12	0.965(5)
O-h	0	0	0.201886	4	0.644(7)
H	0	0	0.057462	4	0.644(7)

600°C Refined stoichiometry: $Ca_{9.61(3)}P_{6.07(3)}O_{26.0(1)}(OH)_{2.61(2)}$; Ca/P: 1.58(1); R_{wp} = 3.88%, R_{exp} = 1.36%

Atoms	*x/a*	*y/b*	*z/c*	*M*	*N*
Ca(1)	0.3333	0.6667	0.0017(5)	4	0.914(4)
Ca(2)	0.25572(24)	0.99784(27)	0.25	6	0.992(4)
P	0.4009(5)	0.3666(5)	0.25	6	1.012(5)
O(1)	0.2996(11)	0.4586(8)	0.25	6	1.03(1)
O(2)	0.5989(6)	0.4791(13)	0.25	6	1.38(1)
O(3)	0.3337(5)	0.2456(4)	0.0504(5)	12	0.967(4)
O-h	0	0	0.201886	4	0.653(6)
H	0	0	0.057462	4	0.653(6)

500°C Refined stoichiometry: $Ca_{9.80(3)}P_{6.26(4)}O_{26.0(2)}(OH)_{2.52(3)}$; Ca/P: 1.57(1); R_{wp} = 3.96%, R_{exp} = 1.24%

Atoms	*x/a*	*y/b*	*z/c*	*M*	*N*
Ca(1)	0.3333	0.6667	0.0060(8)	4	0.935(5)
Ca(2)	0.24442(33)	0.9855(4)	0.25	6	1.010(4)
P	0.3953(8)	0.3717(6)	0.25	6	1.043(6)
O(1)	0.2970(14)	0.4608(11)	0.25	6	1.009(12)
O(2)	0.6032(7)	0.4847(14)	0.25	6	1.412(15)
O(3)	0.3321(6)	0.2443(5)	0.0508(6)	12	0.952(5)
O-h	0	0	0.201886	4	0.629(7)
H	0	0	0.057462	4	0.629(7)

The findings suggest that the successive annealing route better preserves structural OH^- while facilitating controlled carbonate loss. By contrast, direct high-temperature calcination can either retain CO_3^{2-} as a surface contaminant or completely eliminate it, depending on pre-treatment.

The combined acid-base treatment and stepwise annealing adopted in this study appear to allow partial CO_3^{2-} incorporation into the HAp lattice before it is gradually removed at elevated temperatures, offering a tunable balance between substitution and crystallinity.

3.4. SEM analysis

The SEM images in Figure 5 (panels a–h) illustrate the morphological evolution of HAp powders extracted from fish scales following alkali pre-treatment and subsequent annealing at different temperatures. The images, arranged in increasing temperature from top to bottom, provide insights into particle growth, crystallinity, and densification trends under different thermal protocols.

The alkali-treated powder (panel a) exhibits loosely aggregated clusters with irregular shapes and rough surfaces, indicative of low crystallinity and the presence of residual organic material.
Mild heating at 320°C (A-320, panel b) leads to slightly more compact clusters, with small particles beginning to coalesce through early-stage necking and inter-particle bonding. At 500°C (panel c), a more distinct spherical morphology emerges, with noticeable particle fusion forming denser clusters, though clear crystallographic facets are still absent. By 600°C (panel d), particle boundaries become more distinct, averaging 75 ± 26 nm in size, but well-defined faceting remains limited.

At 700°C (A-700, panel e), grains coarsen into near-spherical or elliptical shapes with smoother surfaces, early faceting, and reduced porosity. The clearer grain boundaries and an average grain size of 217 ± 70 nm suggest improved crystallization, though complete hexagonal faceting is not yet achieved. At 800°C (panel f), particles exhibit well-defined hexagonal facets, a hallmark of enhanced crystallinity and reduced structural distortions. Grain diameters range from 200–400 nm, with one facet measuring 248.5 ± 14.9 nm. The formation of hexagonal morphologies indicates significant structural reorganization and greater crystallinity, consistent with the observed improvements in the XRPD data.

In contrast, direct calcination at 700°C (AD-700, panel g) results in tightly fused grains with reduced internal porosity, forming dense agglomerates a few hundred nanometers in size. Single-step calcination at 800°C (AD-800, panel h) produces the largest and most consolidated grains (>300–400 nm), with less distinct particle boundaries due to extensive sintering compared to A-800. Internal pores are largely eliminated, indicating an advanced stage of densification. These results align with previous studies [17], [33], where direct calcination led to significant particle aggregation and irregular morphologies, emphasizing the need for a controlled thermal strategy.

BET surface area analysis supports these morphological trends. The 'Alkali' sample—without heat treatment—exhibits the highest surface area (140.46 m^2/g), consistent with its fine, porous texture. Upon heating, surface area declines progressively: A-600 shows a reduced value of 3.11 m^2/g, while A-800 drops further to 1.78 m^2/g, indicating particle growth and densification. The directly annealed AD-800 sample presents the lowest surface area at 0.73 m^2/g, correlating with extensive sintering and minimal porosity.

Overall, direct calcination results in partial agglomeration, while successive annealing yields smaller, more crystalline particles while preserving the powder form. Both methods achieve high density with sufficient heat, but multi-step processing better controls grain growth, which could enhance mechanical properties. The present findings further confirm that stepwise annealing, combined with intermediate grinding, prevents excessive sintering and allows for more uniform particle coalescence, a feature absent in direct calcination methods previously reported in [17, 33].

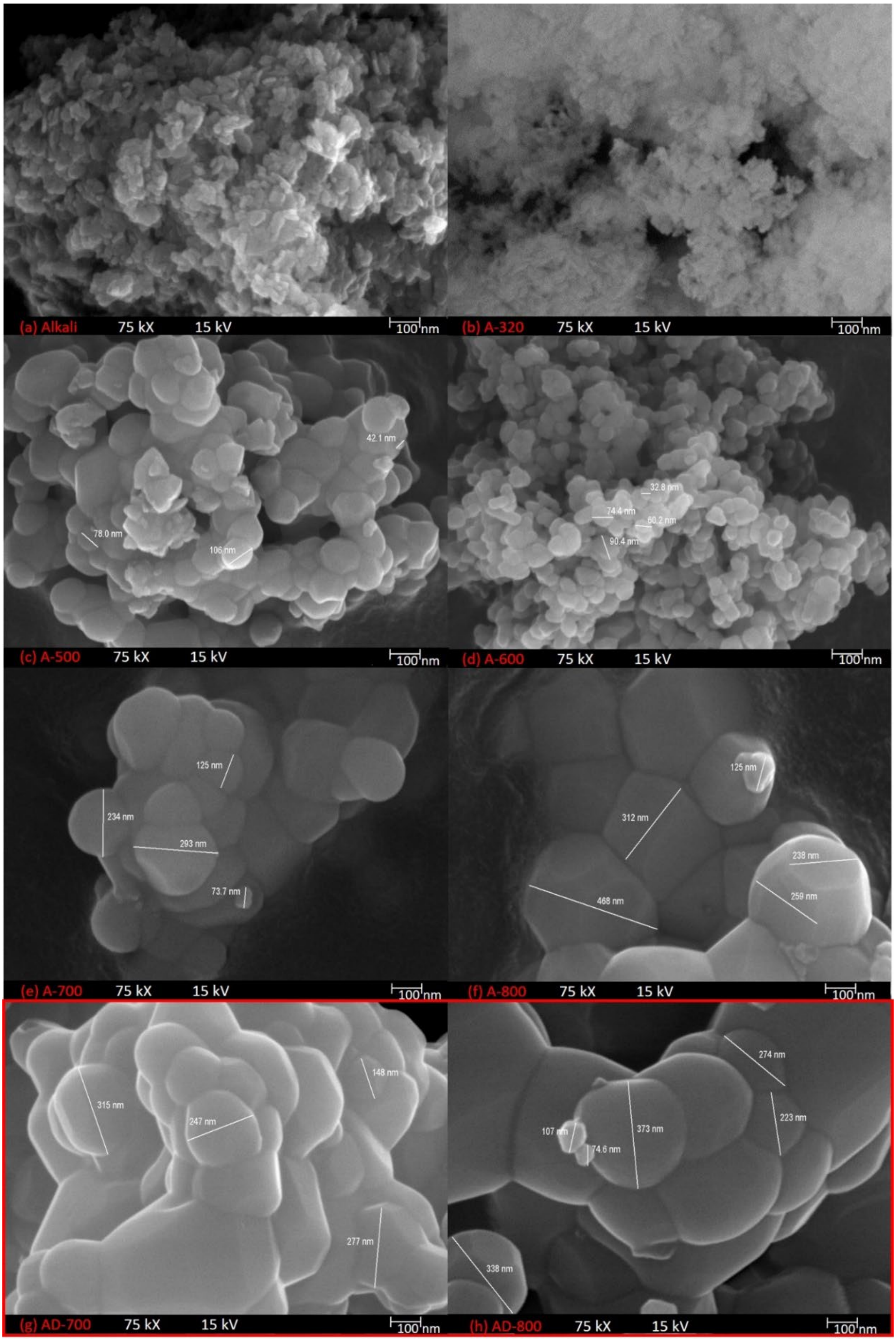

Figure 5. SEM images of HAp powders obtained after alkali pre-treatment and successive annealing, arranged from top to bottom in increasing temperature: (a) alkali-treated sample without thermal treatment: Alkali, (b) 320°C (A-320), (c) 500°C (A-500), (d) 600°C (A-600), (e) 700°C (A-700). The images at the bottom in red frame are collected on the directly calcined powders: (f) 700°C (AD-700) and (g) 800°C (AD-800). All images are collected with a magnification of 75.00 kX and 15 kV

3.5. EDS semi-quantitative analysis

In addition to SEM observations, EDS was used to verify the elemental composition of selected HAp powders, focusing on potential incorporation of minor dopants such as Mg and CO_3^{2-}. Figure 6 shows representative SEM images, EDS spectra, and elemental maps for A-800 and AD-800 samples. Due to its semi-quantitative nature, particularly for light elements (e.g., C, Na, Mg), EDS often registers trace elements as not 'detected' in point analyses (Figure 6b, e), though mapping (Figure 6c, f) reveals localized Mg-rich zones. This discrepancy highlights both the detection limit and the non-uniform distribution of Mg

Despite these limitations, the presence of carbon in the EDS spectra (albeit semi-quantitatively) aligns with the carbonate bands observed in FTIR. This suggests partial CO_3^{2-} substitution in the HAp lattice rather than mere surface contamination. However, EDS alone cannot definitively confirm the site of substitution (A-type vs. B-type) or distinguish from potential surface contamination. Consequently, Rietveld refinement (Section 3.2) was employed to test for CO_3^{2-} in phosphate sites (i.e., A-type) and for potential Mg^{2+} substitution at Ca positions. While lab-based XRPD has limited sensitivity to light elements like C, and minor doping can be difficult to quantify precisely, FTIR and EDS collectively suggest that small amounts of Mg and CO_3^{2-} can incorporate into the HAp lattice at moderate temperatures.

Moreover, Ca/P ratios from EDS may exceed the stoichiometric value (1.67) due to surface effects and quantification limits, whereas Rietveld refinement offers a chemically constrained estimation, despite limitations for light elements of XRPD. Overall, the combination of FTIR and EDS confirms a partially carbonated HAp structure, especially in successively annealed samples. This suggests that stepwise heating facilitates the retention of volatile substituents, while direct annealing favors their loss.

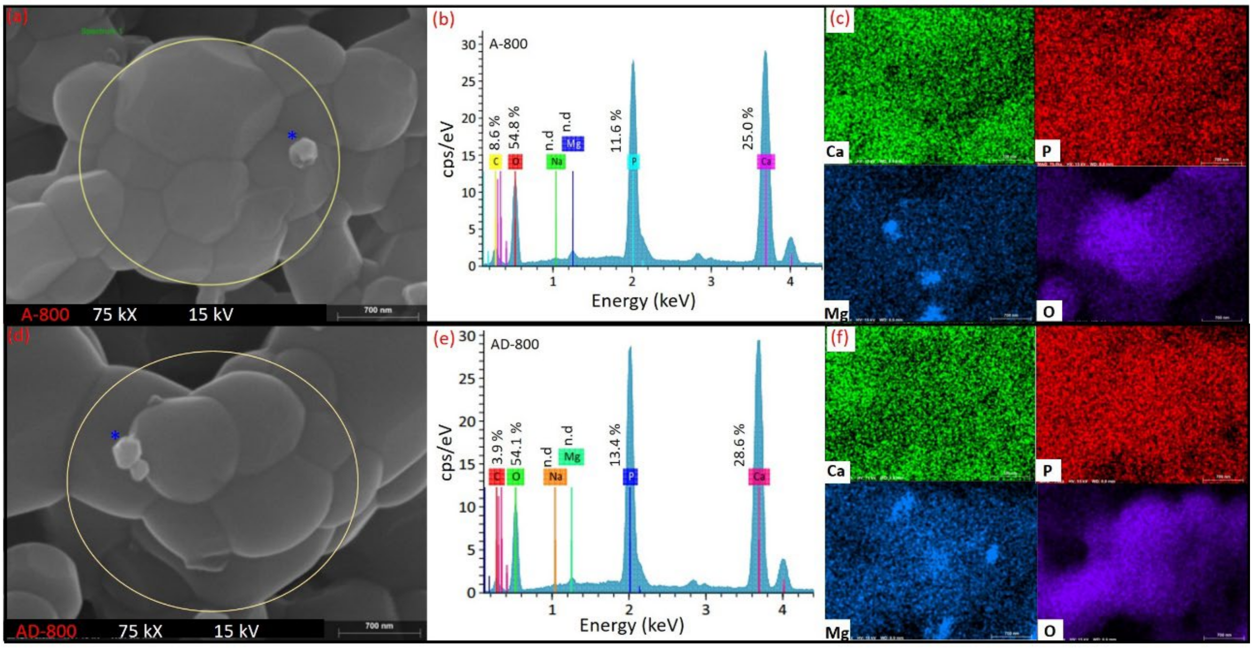

Figure 6. (a, d): SEM images of HAp powders after alkali pre-treatment and successive annealing at 800 °C (a: A-800) and direct annealing at 800 °C (d: AD-800). The yellow circles indicate the regions selected for EDS analysis. (b, e): Corresponding EDS spectra, listing semi-quantitative elemental compositions in atomic %. (c, f): EDS maps for Ca, P, O, and Mg. Although Na and Mg were below the detection limit in spot analyses, the mapping suggests localized Mg (blue star in panels a and d), indicating trace-level incorporation in these samples.

4. Discussion

Successive annealing provides a controlled thermal strategy for crystallizing biogenic HAp, enabling gradual microstrain relaxation and defect reduction while mitigating excessive grain growth. In contrast, direct one-step calcination often results in coarser grains, significant particle agglomeration, and even secondary phase formation due to the rapid and unregulated input of thermal energy [61].

For instance, nano-HAp calcined at 1200 °C has been shown to grow from 10–20 nm to 300–400 nm crystallites [32]. In the current study, intermediate grinding applied between successive heating stages disrupted agglomerates and re-exposed fresh surfaces, thereby preventing uncontrolled crystal overgrowth. As a result, stepwise thermal treatment combined with grinding yielded finer, more uniform particles with narrower size distributions—morphological traits favorable for biomedical and catalytic applications [62]. The gradual thermal ramping also facilitated stepwise removal of residual organic material, while preventing premature sintering. Direct high-temperature (high-T) annealing can cause early densification, locking in residual strain and organic remnants, ultimately producing suboptimal microstructures as shown in previous studies [17].

In contrast, this study shows that even the as-prepared alkali-treated powder without any thermal annealing is phase-pure, and remains so throughout annealing from 320 °C to 800 °C. This consistent phase purity across a broad temperature range underscores the efficacy of the alkali pre-treatment and thermal optimization in stabilizing the HAp structure and avoiding secondary phase formation such as β-TCP or CaO, typically observed at temperatures above 1000 °C [32, 44].

A previous study on HAp powders derived from salmon bone examined the effects of calcining bio-calcium powders with and without alkali pre-treatment at 600°C and 900°C [40]. Their XRPD analysis indicated that in the absence of alkali pre-treatment, a secondary β-TCP phase formed alongside HAp, whereas the alkali-treated sample remained as a single-phase HAp. This further reinforces the role of alkali pre-treatment in stabilizing phase purity and mitigating secondary phase formation during thermal processing.These results align with the present study and previous reports where magnesium whitlockite was found to be present as a secondary phase in direct calcination, with a weight fraction of 15.9(1)% in [17] and 16.7(1)% in [33].

Compared to the SEM images reported in [40], where the powders exhibited significant agglomeration with indistinct grain boundaries, the present study demonstrates a more refined microstructure with well-defined particle morphology. Samples subjected to direct calcination at 900°C in their work show extensive clustering and irregular particle distribution. In contrast, even at a significantly lower temperature of 700°C, the successively annealed powders in this study exhibit superior morphological refinement, with distinct grain boundaries and reduced agglomeration. Additionally, while their alkali-treated powders exhibit some degree of refinement, the overall morphology remains less defined than in the present study, particularly at 800°C, where clear faceted structures emerge.

Notably, even at 600°C (A-600), the HAp powder in this study already displays clearer grain boundaries and a more uniform particle distribution compared to the 900°C samples in [40]. This indicates that high-T calcination alone does not necessarily yield improved morphology. Instead, the stepwise annealing approach with intermediate grinding used here promotes crystallinity and particle uniformity while avoiding excessive grain growth and hard agglomeration. These findings underscore the effectiveness of controlled thermal processing in achieving a highly refined HAp microstructure at significantly lower temperatures. A single high-T calcination may also sinter the particles too early, collapsing inter-particle pores and complicating post-processing. By pausing to grind at moderate temperatures, the present method keeps the powder free-flowing, narrows the particle size distribution [63], and reduces the risk of creating dense aggregates.

The phenomenon of coalescence—the merging of adjacent nanocrystals into larger, more ordered structures—has a major influence on the morphology, crystallinity, and stability of biogenic HAp. A study on bovine bone HAp [64] reported coalescence beginning around 520°C, yielding higher crystallinity, reduced lattice strain, and an expanded unit cell. These observations align well with the overall trends of improved ordering and structural evolution seen in this study. By incrementally heating alkali-treated biogenic HAp from 500°C to 800°C, SEM images from this study show a similar evolution: at 500°C, particles start to coalesce into denser clusters; at 600°C, neck formation and initial crystal growth emerge; at 700°C, significant coalescence yields partially faceted particles; and by 800°C, well-defined hexagonal crystals are visible.

Notably, porcine bone–derived HAp often requires ≥1000–1200 °C to achieve such faceted hexagonal morphologies [65]. In contrast, the multi-step annealing + grinding approach enables this advanced crystallinity at only 800 °C, cutting thermal requirements and avoiding oversintering. This lower threshold preserves material integrity (e.g., preventing secondary phases or heavy densification) and is advantageous when highly crystalline, faceted particles are sought—such as in biomedical coatings or adsorbent applications. Intermediate grinding between annealing stages is pivotal for breaking agglomerates and enabling nanocrystals to reorganize along preferred crystallographic orientations. The absence of faceted structures in previous studies at similar or higher temperatures highlights how integral intermediate grinding is to achieving a high level of refinement. By systematically promoting crystal growth while avoiding large agglomerates, this strategy yields highly faceted, homogeneous hexagonal particles at 800 °C—an approach that significantly advances the synthesis of biogenic HAp from fish scales for various biomedical and environmental applications.

From a porosity perspective, stepwise annealing helps preserve internal pore networks and surface area. Literature shows a sharp decrease in BET surface area for HAp—from ~70–80 m^2/g at 400 °C to ~5–7 m^2/g at 1000 °C—due to sintering and crystallite coalescence [61]. In this study, BET surface area measurements follow a similar trend. The alkali-treated and A-600 powders retain higher surface areas compared to A-800 and AD-800, supporting the idea that prolonged, single-step calcination collapses pore networks. SEM observations further corroborate this trend, with denser particle fusion and pore elimination seen in AD samples. These findings highlight a typical trade-off in thermally treated bioceramics: increased crystallinity at elevated temperatures often results in diminished surface area. Therefore, optimizing this balance is essential, especially when designing HAp materials for surface-dependent applications such as adsorption or catalysis.

These findings underscore that successive annealing is especially beneficial for applications that require nanostructured or porous HAp—such as bone scaffolds and adsorption systems—where high surface area and interconnected porosity are critical [61, 66]. Meanwhile, direct high-temperature calcination may still be preferable for producing dense HAp coatings or implants that benefit from reduced porosity [32]. Ultimately, the thermal route should be selected based on the desired structural characteristics and end-use application

5. Conclusions

This study presents a strategically optimized approach for synthesizing high-purity hydroxyapatite (HAp) from fish scales by integrating successive annealing with intermittent grinding. This multi-step thermal route surpasses the limitations of direct calcination by systematically enhancing crystallinity, minimizing structural imperfections, and enabling the formation of well-defined hexagonal facets at a relatively low temperature. In contrast to single-step high-temperature calcination—which often leads to uncontrolled grain growth, premature densification, and secondary phase formation—the stepwise method ensures phase purity while preserving intrinsic nanostructure of HAp.

The combined insights from Rietveld refinement, FTIR, SEM, and EDS analyses highlight how controlled thermal processing promotes structural ordering, eliminates phases such as magnesium whitlockite, and facilitates partial carbonate retention. Intermediate grinding further supports uniform coalescence and pore preservation, critical for maintaining interconnected micro-/mesoporosity.

This tailored synthesis route offers a cost-effective, scalable pathway for producing structurally refined biogenic HAp while exemplifying sustainable valorization of fish scale waste. Rather than implying immediate readiness, the material holds strong potential for applications where crystallinity and porosity are key—such as biomedical coatings, high-surface-area adsorbents, and catalytic materials. Future studies should focus on evaluating biological compatibility and catalytic performance to validate practical applicability and to optimize the balance between crystallinity and surface area.

Article Information Form

Acknowledgments

The author sincerely thanks Tabii Soğuk Hava Depoculuk Limited Co. and Kocamanlar Seafood for providing the fish scales used in this study.

The Declaration of Conflict of Interest/ Common Interest

No conflict of interest or common interest has been declared by authors.

Artificial Intelligence Statement

No artificial intelligence tools were used while writing this article.

Copyright Statement

References

[1] D. Coppola, C. Lauritano, F. Palma Esposito, G. Riccio, C. Rizzo, D. de Pascale, “Fish waste: From Problem to valuable resource,” Marine Drugs, vol. 19, no. 2, 2021.

[2] R. Cooney, DB de Sousa, A. Fernandez-Rios, S. Mellett, N. Rowan, AP Morse, M Hayes, J. Laso, E. Clifford, “A circular economy framework for seafood waste valorisation to meet challenges and opportunities for intensive production and sustainability,” Journal of Cleaner Production, vol. 392, p. 136283, 2023.

[3] T. Safronova, V. Vorobyov, N. Kildeeva, T. Shatalova, O. Toshev, Y. Filippov, A. Dmitrienko, O. Gavlina, O. Chernega, E. Nizhnikova, “Inorganic powders prepared from fish scales,” Ceramics Switzerland, vol. 5, no. 3, pp. 484–498, 2022.

[4] S. V Dorozhkin, Calcium orthophosphates: Applications in nature, biology, and medicine, first ed., Jenny Stanford Publishing, New York, 2012.

[5] S. V Dorozhkin, “Calcium orthophosphates and human beings: A historical perspective from the 1770s until 1940,” Biomatter, vol. 2, no. 2, pp. 53–70, 2012.

[6] S. V Dorozhkin, “Calcium orthophosphates ($CaPO_4$): Occurrence and properties,” Progress in Biomaterials, vol. 5, no. 1, pp. 9–70, 2016.

[7] S. Weiner, H. D. Wagner, “The material bone: Structure-mechanical function relations,” Annual Review of Materials Research, vol. 28, pp. 271–298, 1998.

[8] P. W. Brown, B. Constantz, Hydroxyapatite and related materials, first ed., CRC press, Florida, 1994.

[9] W. Suchanek, M. Yoshimura, “Processing and properties of hydroxyapatite-based biomaterials for use as hard tissue replacement implants,” Journal of Materials Research, vol. 13, no. 1, pp. 94–117, 1998.

[10] R. Murugan, S. Ramakrishna, “Development of nanocomposites for bone grafting,” Composite Science Technology, vol. 65, no. 15, pp. 2385–2406, 2005.

[11] N. Eliaz, N. Metoki, “Calcium phosphate bioceramics: A review of their history, structure, properties, coating technologies and biomedical applications,” Materials (Basel, Switzerland), vol. 10, no. 4, 2017.

[12] J. Jeong, J. H. Kim, J. H. Shim, N. S. Hwang, C. Y. Heo, “Bioactive calcium phosphate materials and applications in bone regeneration,” Biomaterials Research, vol. 23, no. 1, 2019.

[13] K. Sato, “Mechanism of hydroxyapatite mineralization in biological systems,” Journal of the Ceramic Society of Japan, vol. 115, no. 1338, pp. 124–130, 2007.

[14] T. Kokubo, Bioceramics and their clinical applications, first ed., Woodhead Publishing, 2008.

[15] K. Allam, A. El Bouari, B. Belhorma, L. Bih, “Removal of methylene blue from water using hydroxyapatite submitted to microwave irradiation,” Journal of Water Resource and Protection, vol. 8, no. 3, pp. 358–371, 2016.

[16] R. Verma, S. R. Mishra, V. Gadore, M. Ahmaruzzaman, “Hydroxyapatite-based composites: Excellent materials for environmental remediation and biomedical applications,” Advance Colloid Interface Science, vol. 315, p. 102890, 2023.

[17] H. E. Okur, “Rietveld refinement-based structural analysis of biogenic hydroxyapatite and its PVA composite for dye removal,” Materials Today Communucations, vol. 43, p. 111723, 2025.

[18] A. S. Posner, A. Perloff, A. F. Diorio, “Refinement of the hydroxyapatite structure,” Acta Crystallography, vol. 11, no. 4, pp. 308–309, 1958.

[19] J. C. Elliott, P. E. Mackie, R. A. Young, “Monoclinic hydroxyapatite,” Science, vol. 180, no. 4090, pp. 1055–1057, 1973.

[20] P. W. Brown, R. I. Martin, “An Analysis of Hydroxyapatite Surface Layer Formation,” The Journal of Physical Chemistry B, vol. 103, no. 10, pp. 1671–1675, 1999.

[21] S. V. Dorozhkin, M. Epple, “Biological and medical significance of calcium phosphates,” Angewandte Chemie nternational ed. in English, vol. 41, no. 17, pp. 3130–3146, 002.

[22] S.-C. Liou, S.-Y. Chen, H.-Y. Lee, J.-S. Bow, “Structural characterization of nano-sized calcium deficient apatite powders,” Biomaterials, vol. 25, no. 2, pp. 189–196, 2004.

[23] Y. Sekine, Y Sekine, R. Motokawa, N. Kozai, T. Ohnuki, D. Matsumura, T. Tsuji, R. Kawasaki, K. Akiyoshi, “Calcium-deficient hydroxyapatite as a potential sorbent for strontium,” Scientific Reports, vol. 7, no. 1, p. 2064, 2017.

[24] M. Sadat-Shojai, M.-T. Khorasani, E. Dinpanah-Khoshdargi, A. Jamshidi, “Synthesis methods for nanosized hydroxyapatite with diverse structures,” Acta Biomaterials, vol. 9, no. 8, pp. 7591–7621, 2013.

[25] P. O. Etinosa, O. A. Osuchukwu, EO Anisiji, M. Y Lawal, SA Mohammed, I. O Isaac, P. G. Oni, “In-depth review of synthesis of hydroxyapatite biomaterials from natural resources and chemical regents for biomedical applications,” Arabian Journal of Chemistry, vol. 17, no. 12, 2024.

[26] S. M. Londoño-Restrepo, C. F. Ramirez-Gutierrez, A. del Real, E. Rubio-Rosas, M. E. Rodriguez-García, “Study of bovine hydroxyapatite obtained by calcination at low heating rates and cooled in furnace air,” Journal of Materials Science, vol. 51, no. 9, pp. 4431–4441, 2016.

[27] S. M. Londono-Restrepo, R. Jeronimo-Cruz, E. Rubio-Rosas, M. E. Rodriguez-Garcia, “The effect of cyclic heat treatment on the physicochemical properties of bio hydroxyapatite from bovine bone,” Journal od Materials Science-Materials in Medicine, vol. 29, no. 5, May 2018.

[28] S. M. Londoño-Restrepo, R. Jeronimo-Cruz, B. M. Millán-Malo, E. M. Rivera-Muñoz, M. E. Rodriguez-García, “Effect of the nano crystal size on the x-ray diffraction patterns of biogenic hydroxyapatite from human, bovine, and porcine bones,” Scientific Reports, vol. 9, no. 1, p. 5915, 2019.

[29] N. A. S. Mohd Pu’ad, P. Koshy, H. Z. Abdullah, M. I. Idris, T. C. Lee, “Syntheses of hydroxyapatite from natural sources,” Heliyon, vol. 5, no. 5, p. e01588, 2019.

[30] P. A. Forero-Sossa, I. U. Olvera-Alvarez, J. D. Salazar-Martinez, D. G. Espinosa-Arbelaez, B. Segura-Giraldo, A. L. Giraldo-Betancur, “Biogenic hydroxyapatite powders: Effects of source and processing methodologies on physicochemical properties and bioactive response,” Materials Characterization, vol. 173, Mar. 2021.

[31] P. Arokiasamy, M. M. A. B. Abdullah, S. Z. Abd Rahim, S. Luhar, A. V. Sandu, N. H. Jamil, M. Nabiałek, “Synthesis methods of hydroxyapatite from natural sources: A review,” Ceramics International, vol. 48, no. 11, pp. 14959–14979, 2022.

[32] A. Kurzyk, A. Szwed-Georgiou, J. Pagacz, A. Antosik, P. Tymowicz-Grzyb, A. Gerle, P. Szterner, “Calcination and ion substitution improve physicochemical and biological properties of nanohydroxyapatite for bone tissue engineering applications.,” Scientific Reports, vol. 13, no. 1, p. 15384, Sep. 2023.

[33] H. E. Okur, “Air-exposure-driven color and optical variations in hydroxyapatite extracted from fish scales,” Sakarya University Journal of Science, vol. 29, no. 1, pp. 125–139, 2025.

[34] Y. Harada, O.; Hasegawa, “Extraction method and extraction apparatus of collagen, production method and production apparatus of hydroxyapatite, and collagen-containing aqueous extract and hydroxyapatite,” Patent JP No. JP2008285456A, 27 November 2008.

[35] X. Li, L. Yang, Y. Yao, T. Lin, Y. Chen, L. Xue, “Comprehensive extraction method of collagen, hydroxyapatite and protein in fish scales,” Patent CN No. 107056933, 18 August 2017.

[36] F. Liu, Y. Ji, S. Zhang, L. Yang, “Method for extracting hydroxyapatite and collagen from fish scales by using deep eutectic solvent,” Patent CN No. 111302319, 19 June 2020.

[37] Z. Zhang, Y. Tu, D. Dai, “Method for Extracting Fish Scale Collagen Protein Peptide Powder and Hydroxyapatite,” Patent CN No. 108949882, 7 December 2018.

[38] S. Kongsri, K. Janpradit, K. Buapa, S. Techawongstien, S. Chanthai, “Nanocrystalline hydroxyapatite from fish scale waste: Preparation, characterization and application for selenium adsorption in aqueous solution,” Chemical Engineering Journal, vol. 215–216, pp. 522–532, 2013.

[39] W. Pon-On, P. Suntornsaratoon, N. Charoenphandhu, J. Thongbunchoo, N. Krishnamra, I. M. Tang, “Hydroxyapatite from fish scale for potential use as bone scaffold or regenerative material,” Materials Science and Engineering: C, vol. 62, pp. 183–189, 2016.

[40] A. T. Idowu, S. Benjakul, S. Sinthusamran, T. Sae-leaw, N. Suzuki, Y Kitani, P. Sookchoo, “Effect of alkaline treatment on characteristics of bio-calcium and hydroxyapatite powders derived from salmon bone,” Applied Sciences, vol. 10, no. 12, 2020.

[41] S. Mondal, S. Mahata, S. Kundu, B. Mondal, “Processing of natural resourced hydroxyapatite ceramics from fish scale,” Advances in Applied Ceramics, vol. 109, no. 4, pp. 234–239, Apr. 2010.

[42] I. Zainol, N. M. Alwi, M. Z. Abidin, H. M. Z. Haniza, M. S. Ahmad, A. Ramli, “Physicochemical properties of hydroxyapatite extracted from fish scales,” in Advancement of Materials and Nanotechnology II, in Advanced Materials Research, vol. 545. Trans Tech Publications Ltd, 2012, pp. 235–239.

[43] N. H. Abdullah, “Preparation and characterization of calcium hydroxyphosphate (hydroxyapatite) from tilapia fish bones and scales via calcination method,” in Development and Investigation of Materials Using Modern Techniques II, in Materials Science Forum,

vol. 1010, Trans Tech Publications Ltd, 2020, pp. 596–601.

[44] T. Eknapakul, S. Kuimalee, W. Sailuam, S. Daengsakul, N. Tanapongpisit, P. Laohana, W. Saenrang, A. Bootchanont, A. Khamkongkaeo, R. Yimnirun, “Impacts of pre-treatment methods on the morphology, crystal structure, and defects formation of hydroxyapatite extracted from Nile tilapia scales,” Royal Society of Chemistry Advances, vol. 14, no. 7, pp. 4614–4622, 2024.

[45] M. Ozawa, S. Suzuki, “Microstructural development of natural hydroxyapatite originated from fish-bone waste through heat treatment,” Journal of American Ceramic Society, vol. 85, no. 5, pp. 1315–1317, 2002.

[46] H. E. Okur, R. H. Colman, Y. Takabayashi, P. Jeglič, Y. Ohishi, K. Kato, D. Arčon, Y Kubota, K. Prassides, “Fulleride superconductivity tuned by elastic strain due to cation compositional disorder,” Cheical Sciences, vol. 15, no. 40, pp. 16485–16493, 2024.

[47] C. F. Ramirez-Gutierrez, S. M. Londoño-Restrepo, A. del Real, M. A. Mondragón, M. E. Rodriguez-García, “Effect of the temperature and sintering time on the thermal, structural, morphological, and vibrational properties of hydroxyapatite derived from pig bone,” Ceramics International, vol. 43, no. 10, pp. 7552–7559, 2017.

[48] A. C. Larson and R. Von Dreele, “General Structure Analysis System (GSAS),” Los Alamos National. Laboratory LAUR, pp. 86–748, 2004.

[49] P. Thompson, D. E. Cox, J. B. Hastings, “Rietveld refinement of debye-scherrer synchrotron X-ray data from A1203,” Journal of Applied Crystallography, vol. 20, no. 2, pp. 79–83, 1987.

[50] C. J. Howard, “The approximation of asymmetric neutron powder diffraction peaks by sums of Gaussians,” Journal of Applied Crystallography, vol. 15, no. 6, pp. 615–620, 1982.

[51] J. Laugier, B. Bochu, “LMGP-Suite of Programs for the interpretation of X-ray Experiments,” 1999, ENSP/Laboratoire des Matériaux et du Génie Physique.

[52] K. Sudarsanan, R. A. Young, “Significant precision in crystal structural details. Holly Springs hydroxyapatite,” Acta Crystallographica Section B, vol. 25, no. 8, pp. 1534–1543, 1969.

[53] E. Hosseinzadeh, M. Davarpanah, N. H. Nemati, S. A. Tavakoli, “Fabrication of a hard tissue replacement using natural hydroxyapatite derived from bovine bones by thermal decomposition method,” International Journal of Organ Transplantation Medicine, vol. 5, no. 1, pp. 23–31, 2014.

[54] R. X. Sun, Y. Lv, Y. R. Niu, X. H. Zhao, D. S. Cao, J. Tang, J., K. Z. Chen, “Physicochemical and biological properties of bovine-derived porous hydroxyapatite/collagen composite and its hydroxyapatite powders,” Ceramics International, vol. 43, no. 18, pp. 16792–16798, 2017.

[55] G. Aydin, P. Terzioğlu, H. Öğüt, A. Kalemtas, “Production, characterization, and cytotoxicity of calcium phosphate ceramics derived from the bone of meagre fish, Argyrosomus regius,” Journal of the Australian Ceramic Society, vol. 57, no. 1, pp. 37–46, 2021.

[56] R. M. Wilson, J. C. Elliott, S. E. P. Dowker, “Rietveld refinement of the crystallographic structure of human dental enamel apatites,” American Mineralogist, vol. 84, no. 9, pp. 1406–1414, 1999.

[57] J. M. Stutman, J. D. Termine, A. S. Posner, “Vibrational spectra and structure of the phosphate ion in some calcium phosphates,” Transactions of the New York Academy of Sciences, vol. 27, no. 6 Series II, pp. 669–675, 1965.

[58] D. W. Holcomb, R. A. Young, “Thermal decomposition of human tooth enamel.,” Calcified Tissue International, vol. 31, no. 3, pp. 189–201, 1980.

[59] M. E. Fleet, X. Liu, “Coupled substitution of type A and B carbonate in sodium-bearing apatite,” Biomaterials, vol. 28, no. 6, pp. 916–926, 2007.

[60] J. C. Elliott, “Structure, crystal chemistry and density of enamel apatites,” in Ciba Foundation Symposium 205 - Dental Enamel, John Wiley & Sons Ltd, pp. 54–72.

[61] N. Patel, I. R. Gibson, S. Ke, S. M. Best, W. Bonfield, “Calcining influence on the powder properties of hydroxyapatite,” Journal of materials science. Materials in medicine, vol. 12, no. 2, pp. 181–188, 2001.

[62] S. Ramesh, C. J. Gan, L. T. Bang, A .Niakan, C. Y. Tan, J. Purbolaksono, H. Chandran, B. K Yap, W.D. Teng, “Effects of two-step sintering on the properties of hydroxyapatite bioceramic,” Journal of Ceramic Processing Research, vol. 16, no. 6, pp. 683–689, 2015.

[63] H. Y. Juang, M. H. Hon, “Effect of calcination on sintering of hydroxyapatite,” Biomaterials, vol. 17, no. 21, pp. 2059–2064, 1996.

[64] D. F. Cañon-Davila, A. M. Castillo-Paz, S. M. Londoño-Restrepo, H. Pfeiffer, R. Ramirez-Bon, and M. E. Rodriguez-Garcia, “Study of the coalescence phenomena in biogenic nano-hydroxyapatite produced by controlled calcination processes at low temperature,” Ceramics International, vol. 49, no. 11, Part A, pp. 17524–17533, 2023.

[65] P. A. Forero-Sossa, J. D. Salazar-Martínez, A. L. Giraldo-Betancur, B. Segura-Giraldo, E. Restrepo-Parra, “Temperature effect in physicochemical and bioactive behavior of biogenic hydroxyapatite obtained from porcine bones,” Scientific Reports, vol. 11, no. 1, p. 11069, 2021.

[66] M. Figueiredo, A. Fernando, G. Martins, J. Freitas, F. Judas, H. Figueiredo, “Effect of the calcination temperature on the composition and microstructure of hydroxyapatite derived from human and animal bone,” Ceramics International, vol. 36, no. 8, pp. 2383–2393, 2010.